

Fast and Scalable FFT-Based GPU-Accelerated Algorithms for Hessian Actions Arising in Linear Inverse Problems Governed by Autonomous Dynamical Systems

Sreeram Venkat^{*1}, Milinda Fernando¹, Stefan Henneking¹, and Omar Ghattas¹

¹Oden Institute, The University of Texas at Austin

Abstract

We present an efficient and scalable algorithm for performing matrix-vector multiplications (“matvecs”) for block Toeplitz matrices. Such matrices, which are shift-invariant with respect to their blocks, arise in the context of solving inverse problems governed by autonomous systems, and time-invariant systems in particular. In this article, we consider inverse problems that are solved for inferring unknown parameters from observational data of a linear time-invariant dynamical system given in the form of partial differential equations (PDEs). Matrix-free Newton-conjugate-gradient methods are often the gold standard for solving these inverse problems, but they require numerous actions of the Hessian on a vector. Matrix-free adjoint-based Hessian matvecs require solution of a pair of linearized forward/adjoint PDE solves per Hessian action, which may be prohibitive for large-scale inverse problems, especially when efficient low-rank approximations of the Hessian are not readily available, such as for hyperbolic PDE operators. Time invariance of the forward PDE problem leads to a block Toeplitz structure of the discretized parameter-to-observable (p2o) map defining the mapping from inputs (parameters) to outputs (observables) of the PDEs. This block Toeplitz structure enables us to exploit two key properties: (1) compact storage of the p2o map and its adjoint; and (2) efficient fast Fourier transform (FFT)-based Hessian matvecs. The proposed algorithm is mapped onto large multi-GPU clusters. A detailed roofline performance evaluation demonstrates that the algorithm achieves more than 80 percent of peak bandwidth on an NVIDIA A100 GPU. Excellent weak scaling is shown on TACC’s *Lonestar6* GPU cluster for up to 48 A100 GPUs. For the targeted problems, the implementation executes Hessian matvecs within fractions of a second, orders of magnitude faster than can be achieved by the conventional matrix-free Hessian matvecs via forward/adjoint PDE solves.

^{*}Corresponding author: srvenkat@utexas.edu

1 Introduction

Adjoint-based matrix-free Newton-conjugate-gradient methods are often the gold standard for solution of inverse problems [10, 24]. However, they typically require numerous actions of the Hessian matrix on a vector, each of which amounts to solution of a pair of forward and adjoint problems. For inverse problems governed by partial differential equations (PDEs) with high-rank Hessians, the resulting number of forward/adjoint PDE solves may be computationally prohibitive. In recent years, several methods that address high-rank Hessians have been developed, including those that exploit the pseudo-differential [21, 7], augmented Lagrangian [3], product-convolution [2], H-matrix [4], and point spread function [1] structure of the Hessians of particular classes of inverse problems.

In this paper, we show that the Hessian structure can be particularly well-exploited for Hessians governed by *autonomous systems*. The evolution of such systems with respect to any given input may depend on the system’s current state but does not explicitly depend on the independent variable. Autonomous systems can arise, for example, in the context of inverse problems for time-invariant dynamical systems, which are a subclass of autonomous systems where the independent variable is time [17, 9, 14]. The autonomous system structure then translates into a *shift invariance* of the corresponding discrete system. In particular, with both parameter field and observables defined in space-time, the discrete parameter-to-observable (p2o) map and its adjoint exhibit shift invariance with respect to the time-stepping. The corresponding matrices are *block Toeplitz*. For time-invariant systems, causality additionally implies the p2o map and its adjoint are lower- and upper-triangular block Toeplitz, respectively. Recognizing this structure enables two properties: 1) compact representation of the p2o map and its adjoint, and 2) fast application of the Hessian via scalable multi-GPU fast Fourier transform (FFT)-accelerated matvecs. Compact representation follows directly from the definition of block Toeplitz matrices. Fast matvecs are achieved by embedding the block Toeplitz matrix within a block circulant matrix, which is diagonalized by the discrete Fourier transform (DFT). The matvec then becomes an elementwise vector operation in Fourier space.

These FFT-based Hessian matvecs are implemented effectively on multi-GPU clusters. Moreover, because the FFT is a unitary operator, the action of the adjoint p2o map corresponds to simply applying the complex conjugate in Fourier space, eliminating the need to separately store the Fourier-transformed forward and adjoint maps. Exploiting the triangular block Toeplitz structure in this way yields memory savings proportional to the number of time steps N_t and a computational speedup of $\mathcal{O}(N_t/\log N_t)$. In the context of explicit methods for time-dependent differential equations, the number of time steps is typically very large due to the Courant–Friedrichs–Lewy (CFL) condition, making the savings of the algorithm substantial.

While the classical FFT algorithm for matvecs involving Toeplitz matrices is well known [11], similar algorithms for general block Toeplitz matrices—i.e. block Toeplitz matrices where the blocks themselves do not have any special structure—have yet to be established. Many authors have extended the FFT-based Toeplitz matvec algorithm to block Toeplitz matrices where each block is itself a Toeplitz matrix [18, 5, 16, 12, 26, 25]. These “multilevel-” or “recursive-” Toeplitz matrices arise in scattering problems and optimal surface interpolation [18, 5]. In [8], the authors discuss extensions of factoring algorithms to symmetric positive definite block Toeplitz matrices; however, the block Toeplitz matrices found in inverse problems are usually not even square matrices. The use of GPUs to accelerate computations involving Toeplitz matrices (through FFTs) is also well documented [20], though the extension to general block Toeplitz matrices and the mapping onto multi-GPU clusters to perform large-scale computations is yet to be reported.

The main contributions of this paper are: (1) algorithms for efficient GPU-accelerated FFT-based matvecs of general block Toeplitz matrices as arise in linear inverse problems governed by

autonomous dynamical systems; (2) extension of the algorithms to a multi-GPU framework; (3) detailed roofline performance analysis for the algorithms; (4) strong and weak scalability study for up to 48 GPUs; and (5) complexity analysis of the algorithms for single-GPU and multi-GPU execution. The contributions made in this paper enable efficient and scalable FFT-based Hessian matvecs for solving large-scale inverse problems governed by autonomous dynamical systems. To the best of our knowledge, this is the first attempt at exploiting the block Toeplitz structure for Hessian matvecs arising in inverse problems and their extension to the multi-GPU setting.

2 Motivation and Background

Our motivation comes from the need to perform Hessian matvecs to solve large-scale inverse problems governed by autonomous systems—time-invariant systems in particular. In this paper, we are concerned with systems governed by PDEs. For such problems, we briefly review the structure of the inverse problem and discuss the case of systems with time invariance that give rise to shift-invariant discrete operators [14]. Before presenting our algorithm in Section 3, we also briefly overview the classical FFT-based matvec algorithm for general Toeplitz matrices.

2.1 Linear Time-Invariant Dynamical System

While our algorithm applies to linear autonomous dynamical systems in general, we consider for illustrative purposes the case of a linear time-invariant (LTI) dynamical system of the form

$$\begin{aligned} \frac{\partial u}{\partial t} &= \mathcal{A}u + \mathcal{C}m && \text{in } \Omega \times (0, T), \\ u &= u_0 && \text{in } \Omega \times \{0\}, \\ d &= \mathcal{B}u && \text{in } \Omega \times (0, T), \end{aligned} \tag{1}$$

with appropriate boundary conditions on $\partial\Omega \times (0, T)$, where Ω is the spatial domain, $(0, T)$ is the time domain, $u(x, t)$ is the system’s state with initial state $u_0(x)$, parameter (input) $m(x, t)$ represents the source or forcing of the system and is independent of the state, and both \mathcal{A} and \mathcal{C} are time-invariant differential operators; $d(x, t)$ describes the observables (output) of the system, which are extracted from the state u via a time-invariant observation operator \mathcal{B} .

Consider a discrete version of the LTI system obtained by discretizing (1) in time with a single-step explicit method,¹

$$u_{k+1} = Au_k + Cm_k, \quad k = 0, 1, \dots, N_t - 1, \tag{2}$$

where $u_k \in \mathbb{R}^{N_u}$, $m_k \in \mathbb{R}^{N_m}$, and the discrete time-stepping operator $A \in \mathbb{R}^{N_u \times N_u}$ and $C \in \mathbb{R}^{N_u \times N_m}$ both depend on the particular time-stepping scheme.² Then, using (2) the discretized LTI system can be written as follows:

¹Note that the methodology is easily extended to multi-step explicit and implicit methods.

²For example, forward Euler time-stepping implies A and C respectively spatially discretize $(\mathcal{I} + \Delta t\mathcal{A})$ and $\Delta t\mathcal{C}$, where \mathcal{I} is identity and Δt is the (uniform) time step size.

$$\begin{aligned}
 u_1 &= Au_0 + Cm_0, \\
 u_2 &= Au_1 + Cm_1, \\
 &= A(Au_0 + Cm_0) + Cm_1 = A^2u_0 + A^1Cm_0 + A^0Cm_1, \\
 &\vdots \\
 u_{k+1} &= A^{k+1}u_0 + \sum_{i=0}^k A^iCm_{k-i}, \\
 d_{k+1} &= Bu_{k+1},
 \end{aligned} \tag{3}$$

where $d_k \in \mathbb{R}^{N_d}$ and $B \in \mathbb{R}^{N_d \times N_u}$ is the discrete observation operator.

Without loss of generality, assume homogeneous initial condition $u_0 = 0$. We can then write the discretized LTI system in the following way:

$$\begin{bmatrix} d_1 \\ d_2 \\ \vdots \\ d_{k+1} \\ \vdots \\ d_{N_t} \end{bmatrix} = \begin{bmatrix} BA^0C & & & & \\ BA^1C & BA^0C & & & \\ \vdots & \vdots & \ddots & & \\ BA^kC & BA^{k-1}C & \cdots & BA^0C & \\ \vdots & \vdots & & \vdots & \ddots \\ BA^{N_t-1}C & BA^{N_t-2}C & \cdots & BA^{N_t-(k+1)}C & \cdots & BA^0C \end{bmatrix} \begin{bmatrix} m_0 \\ m_1 \\ \vdots \\ m_k \\ \vdots \\ m_{N_t-1} \end{bmatrix}. \tag{4}$$

We define $F_{ij} := BA^{i-j}C \in \mathbb{R}^{N_d \times N_m}$, $i, j = 1, 2, \dots, N_t, i \geq j$; the LTI system (2) can then be written more compactly as follows:

$$\begin{bmatrix} d_1 \\ d_2 \\ d_3 \\ \vdots \\ d_{N_t} \end{bmatrix} = \begin{bmatrix} F_{11} & 0 & 0 & \cdots & 0 \\ F_{21} & F_{11} & 0 & \cdots & 0 \\ F_{31} & F_{21} & F_{11} & \ddots & \vdots \\ \vdots & \vdots & \ddots & \ddots & 0 \\ F_{N_t,1} & F_{N_t-1,1} & \cdots & F_{21} & F_{11} \end{bmatrix} \begin{bmatrix} m_0 \\ m_1 \\ m_2 \\ \vdots \\ m_{N_t-1} \end{bmatrix}, \tag{5}$$

or very concisely as

$$\mathbf{d} := \mathbf{F}\mathbf{m}. \tag{6}$$

We refer to \mathbf{F} as the (discrete) *parameter-to-observable* (p2o) map; \mathbf{m} is the parameter vector and \mathbf{d} is the vector of observables or data vector. Then,

- $\mathbf{m} \in \mathbb{R}^{N_m N_t}$ with blocks $m_j \in \mathbb{R}^{N_m}$, $j = 1, 2, \dots, N_t$;
- $\mathbf{d} \in \mathbb{R}^{N_d N_t}$ with blocks $d_i \in \mathbb{R}^{N_d}$, $i = 1, 2, \dots, N_t$;
- $\mathbf{F} \in \mathbb{R}^{(N_d N_t) \times (N_m N_t)}$ with blocks $F_{ij} \in \mathbb{R}^{N_d \times N_m}$, $i, j = 1, 2, \dots, N_t$.

It is clear from (5) that the p2o map \mathbf{F} is shift-invariant with respect to its blocks F_{ij} . In particular, \mathbf{F} is *block Toeplitz*. Additionally, time causality implies that \mathbf{F} is block lower-triangular. The next two sections describe how this special structure of \mathbf{F} can be effectively exploited in the context of solving inverse problems.

2.2 Hessian Matvec for Inverse Problems

Given a system of the form (6), we consider the inverse problem of inferring the parameters \mathbf{m} from the observed data \mathbf{d}^{obs} . This inverse problem can be solved by casting it as a quadratic optimization problem of minimizing the regularized data misfit:

$$\min_{\mathbf{m}} J(\mathbf{m}) := \frac{1}{2} \|\mathbf{F}\mathbf{m} - \mathbf{d}^{\text{obs}}\|^2 + \frac{\alpha}{2} \|\mathbf{m}\|_{\mathbf{R}}^2, \quad (7)$$

where $\alpha > 0$ and regularization operator $\mathbf{R} \in \mathbb{R}^{(N_m N_t) \times (N_m N_t)}$ is positive definite. The goal is to minimize the objective $J(\mathbf{m})$ in (7) which, through p2o map \mathbf{F} , is constrained by the LTI system (2). Minimization of (7) defines a linear inverse problem:

$$(\mathbf{F}^*\mathbf{F} + \alpha\mathbf{R})\mathbf{m} = \mathbf{F}^*\mathbf{d}^{\text{obs}}, \quad (8)$$

where \mathbf{F}^* denotes the adjoint of the p2o map,³ and $\mathbf{H} := \mathbf{F}^*\mathbf{F} + \alpha\mathbf{R} \in \mathbb{R}^{(N_m N_t) \times (N_m N_t)}$ is the Hessian.

If the action of the Hessian on a vector is available, the inverse problem (8) can be solved efficiently by iterative methods such as conjugate gradients. When preconditioned by the regularization operator, the number of iterations typically scales with the effective rank of the preconditioned Hessian of the data misfit, $\alpha^{-1}\mathbf{R}^{-1}\mathbf{F}^*\mathbf{F}$, since the resulting operator has the structure of a compact perturbation of the identity [10]. For the iterative solution to be practical, it is paramount that the Hessian matvec can be carried out efficiently at each iteration.

For large-scale inverse problems, the action of the Hessian on a vector is typically formed in a matrix-free way, i.e. \mathbf{H} is never explicitly constructed, since doing so requires either $N_m N_t$ forward solves or $N_d N_t$ adjoint solves, whichever is less expensive. However, each Hessian matvec comes at the cost of a pair of forward and adjoint solves of the governing PDE system, which can be very expensive when performed repeatedly. For the LTI system (2), each forward solve requires N_t applications of the time-stepping forward operator A . Analogously, each adjoint solve requires N_t applications of a time-stepping adjoint operator A^* .⁴ This cost can make solving the inverse problem prohibitively expensive.

For example, consider inverse problem (8) of size $N_d = \mathcal{O}(10^2)$, $N_m = \mathcal{O}(10^6)$, $N_t = \mathcal{O}(10^4)$.⁵ Unless the Hessian has low rank, solving an inverse problem of this size with traditional methods is extremely challenging (indeed, it may require up to $\mathcal{O}(10^6)$ Hessian matvecs, i.e. up to $\mathcal{O}(10^{10})$ applications of the time-stepping forward and adjoint operators A and A^*).

To make this notion more concrete and be able to better compare the computational cost of the conventional approach—the matrix-free Hessian matvec via a pair of forward/adjoint PDE solves—to the proposed method, we estimate the number of floating-point operations (FLOPs) needed to apply the p2o map for a particular example. For estimating FLOPs, we assume values for the number of parameters, time steps, grid points, and other variables, that represent practical large-scale problems including our own target applications. Consider elastic wave propagation in displacement form (e.g. [6]) discretized with a 27-point stencil in a uniformly refined three-dimensional cube

³Note that analogous to the p2o map \mathbf{F} , the adjoint p2o map \mathbf{F}^* is block Toeplitz; however, \mathbf{F}^* is block upper-triangular. Moreover, applying \mathbf{F}^* to a vector involves the adjoint operator A^* of the governing LTI system.

⁴For the LTI system, the cost of applying the adjoint operator is similar to the cost of applying the forward operator.

⁵Large-scale inverse problems for complex physical systems are often data-sparse—i.e. the number of observers (sensors) is limited—while having high-dimensional parameter fields ($N_m \gg N_d$).

with N_g grid points.⁶ The spatial state dimension is $N_u = 3N_g$ (3 degrees of freedom (DOFs) per grid point). We assume that the spatiotemporal parameter field is a (scalar-valued) field spatially discretized on the top surface of the spatial domain, $N_m = N_g^{2/3}$, and observations are taken at a small number of sensors, $N_d \ll N_m$. The cost for applying the spatially discretized PDE operator once is approximately $81N_u$ FLOPs.⁷ With a classic explicit RK4 time-stepping scheme, the spatially discretized operator is applied four times per time step, costing $324N_u$ FLOPs per time step. Each forward (or adjoint) PDE solve involves N_t time steps, so the total cost per PDE solve is approximately $324N_uN_t$ FLOPs. Assuming the number of grid points is $N_g = 10^9$ and the number of time steps is $N_t = 10^4$, each PDE solve costs $9.72 \cdot 10^{15}$ FLOPs or 9.72 petaFLOPs. To estimate the number of PDE solves needed for solving the inverse problem, we have to estimate the effective rank r of the (preconditioned) Hessian. Assuming $N_d = 10^2$ sensors and that we can reconstruct at most 10% of the modes, $r = N_dN_t/10 = 10^5$. Then, solving the inverse problem in the conventional way costs $2r \cdot 9.72 \cdot 10^{15} \approx 1.944 \cdot 10^{21}$ FLOPs or 1944 exaFLOPs.⁸

In the next section, we propose a computationally much more efficient approach for Hessian matvecs that makes solving inverse problems governed by autonomous dynamical systems orders of magnitude cheaper at this scale.

2.3 Inverse Problems Involving Shift-Invariant Systems

Our approach exploits the shift invariance of (5) and trades computer storage for computational efficiency. Assuming the above estimates for N_d , N_m , and N_t , then formally the Hessian \mathbf{H} and the p2o map \mathbf{F} each have $\mathcal{O}(10^{10})$ columns. Clearly, pre-computing and storing these dense matrices naively column-by-column by performing $\mathcal{O}(10^{10})$ matvecs is not a feasible option. However, recognizing the block Toeplitz structure of the p2o map enables two key properties: (1) compact storage of the p2o map and its adjoint; and (2) efficient FFT-based Hessian matvecs. In particular:

- \mathbf{F} can be pre-computed by only N_m forward solves (to obtain the first block column) or N_d adjoint solves (to obtain the last block row) as compared to the naive approach of performing N_mN_t forward solves or N_dN_t adjoint solves;
- \mathbf{F} can be compactly stored in $\mathcal{O}(N_mN_dN_t)$ memory, a savings of $\mathcal{O}(N_t)$;
- \mathbf{F} can be efficiently applied to a vector by a specialized FFT-based matvec algorithm at the cost of $\mathcal{O}(N_mN_dN_t \log N_t)$, a speedup of $\mathcal{O}(N_t/\log N_t)$ over the naive approach;
- \mathbf{F}^* does not need to be computed or stored separately because the same FFT-based matvec algorithm with only minor modifications efficiently applies \mathbf{F}^* to a vector, reducing the cost of the adjoint p2o matvec to $\mathcal{O}(N_mN_dN_t \log N_t)$, as well.

Once the shift-invariant p2o map has been pre-computed and stored compactly, the efficiency of the FFT-accelerated \mathbf{F} and \mathbf{F}^* matvecs implies that the Hessian matvec becomes relatively cheap, because it no longer involves applying the forward or adjoint time-stepping operators. The computational cost of pre-computing \mathbf{F} and \mathbf{F}^* is small compared to the cost of solving the inverse problem using the conventional Hessian matvec method, as we show below.

⁶Discretization with a 27-point stencil is comparable to a first-order hexahedral finite element discretization. Since higher-order discretization makes applying the discretized PDE operator more expensive, the 27-point stencil can be used as a lower bound for the speedup of our method.

⁷Using a 27-point stencil with 3 state DOFs per grid point, each state DOF is connected to (at most) 81 DOFs.

⁸Note that this analysis neglected the cost of applying (or preconditioning with) the regularization operator \mathbf{R} , which is assumed to be significantly cheaper than solving the PDE system.

Using the elastic wave propagation example and estimates from Section 2.2, the one-time cost of pre-computing the p2o operator is $N_d \cdot 9.72 \cdot 10^{15}$ FLOPs = 972 petaFLOPs and requires storing N_d vectors of size $N_m N_t$ which, assuming double precision, is 8 TB of storage in total. The one-time cost for computing the FFTs of the matrix blocks is negligible relative to the cost of pre-computing the operator. The cost of performing FFT-accelerated matvecs of \mathbf{F} and \mathbf{F}^* , which involves a number of different operations (see Section 3), is approximately $8N_m N_d N_t = 8 \cdot 10^{12}$ FLOPs or 8 teraFLOPs,⁹ which is $\sim 1,000\times$ more efficient than the conventional method for each \mathbf{F} or \mathbf{F}^* application. Solving the inverse problem with the FFT-accelerated matvecs thus costs 972 petaFLOPs (one-time setup cost) plus $2r \cdot 8 \cdot 10^{12} = 1.6 \cdot 10^{18}$ FLOPs (10^5 FFT-based matvecs of \mathbf{F} and \mathbf{F}^*), or 2.57 ExaFLOPs in total. This is over $750\times$ more efficient than solving the inverse problem using the conventional way of performing Hessian matvecs described in Section 2.2. We emphasize that the realized efficiency gain will in many cases be much larger, particularly when (1) the PDE time-stepping method uses a much smaller time step for stability (CFL condition) or accuracy than the temporal discretization of parameters and data; (2) the PDE is spatially discretized with a high-order method; or (3) the LTI system describes a multiphysics or mixed problem with a larger number of variables (discretized with many DOFs per grid point).

The resulting savings from performing fast FFT-based Hessian matvecs are important for several reasons: (1) they can enable solving large-scale inverse problems that may otherwise be prohibitively expensive to solve; (2) they can significantly reduce the cost of inverting from many different data vectors, in which case the cost of pre-computing \mathbf{F} and \mathbf{F}^* is easily amortized; and (3) they can make real-time inversion feasible for time-sensitive applications. Moreover, the FFT-based Hessian matvecs are well-suited for GPU-accelerated computation, even when the forward and adjoint problems employ implicit solvers, adaptive mesh refinement, low order discretization, or other methods that are typically not amenable to achieving peak performance on GPUs.

The remainder of this paper addresses the issue of efficiently applying \mathbf{F} and \mathbf{F}^* of the structure (5). Note that while the p2o map is shift-invariant in time (i.e. \mathbf{F} has Toeplitz structure with respect to time steps), the blocks F_{ij} themselves are not assumed to have any special structure and, typically, they are not even square matrices ($N_m \neq N_d$). We assume that *either* \mathbf{F} or \mathbf{F}^* is available in compactly stored form (see Section 3 for details). For a discussion of the broader context of solving inverse problems involving shift-invariant systems, we refer to [14]. This paper focuses on the fast and scalable implementation of the p2o and adjoint p2o matvecs, which are an essential building block for solving such inverse problems. Before describing our method in detail in Section 3, we briefly introduce the well-known FFT-based matvec algorithm for Toeplitz matrices.

2.4 FFT-Based Matvec for Toeplitz Matrices

This section describes the algorithm for computing matvecs of a generic Toeplitz matrix $M_{\text{toep}} \in \mathbb{R}^{n \times n}$ given by

$$M_{\text{toep}} = \begin{bmatrix} m_0 & m_{-1} & \cdots & m_{-(n-1)} \\ m_1 & m_0 & \ddots & \vdots \\ \vdots & \vdots & \ddots & m_{-1} \\ m_{n-1} & m_{n-2} & \cdots & m_0 \end{bmatrix}$$

and a vector $\mathbf{x} \in \mathbb{R}^n$.

⁹The costs are dominated by the SBGEMV (see Section 4, Fig. 1). The coefficient 8 comes from complex-valued operations (6 FLOPs per multiplication, 2 FLOPs per addition).

To compute the matvec $M_{\text{toep}}\mathbf{x}$, the matrix M_{toep} is first embedded inside the circulant matrix $M_{\text{circ}} \in \mathbb{R}^{2n \times 2n}$ given by

$$M_{\text{circ}} := \begin{bmatrix} M_{\text{toep}} & M' \\ M' & M_{\text{toep}} \end{bmatrix} := \left[\begin{array}{ccccc|ccccc} m_0 & m_{-1} & \cdots & \cdots & m_{-(n-1)} & 0 & m_{n-1} & \cdots & m_2 & m_1 \\ m_1 & m_0 & \ddots & & \vdots & m_{-(n-1)} & \ddots & \ddots & & m_2 \\ m_2 & \ddots & \ddots & \ddots & \vdots & \vdots & \ddots & & \ddots & \vdots \\ \vdots & & \ddots & m_0 & m_{-1} & m_{-2} & & \ddots & \ddots & m_{n-1} \\ m_{n-1} & \cdots & \cdots & m_1 & m_0 & m_{-1} & m_{-2} & \cdots & m_{-(n-1)} & 0 \\ \hline 0 & m_{n-1} & \cdots & \cdots & m_1 & m_0 & m_{-1} & \cdots & \cdots & m_{-(n-1)} \\ m_{-(n-1)} & \ddots & \ddots & & m_2 & m_1 & m_0 & \ddots & & \vdots \\ \vdots & \ddots & & \ddots & \vdots & m_2 & \ddots & \ddots & \ddots & \vdots \\ m_{-2} & & \ddots & \ddots & m_{n-1} & \vdots & & \ddots & m_0 & m_{-1} \\ m_{-1} & m_{-2} & \cdots & \cdots & 0 & m_{n-1} & \cdots & \cdots & m_1 & m_0 \end{array} \right]. \quad (9)$$

It is well known [11] that the DFT matrix D diagonalizes the circulant matrix M_{circ} ; that is, $M_{\text{circ}} = (2n)^{-1/2} D^{-1} \text{diag}\left(\widehat{(M_{\text{circ}})_0}\right) D$, where $(M_{\text{circ}})_0$ is the first column of M_{circ} , and $\widehat{\cdot}$ denotes the FFT. So, to compute $M_{\text{toep}}\mathbf{x}$, set $\mathbf{u} := [\mathbf{x} \ \mathbf{0}]^T \in \mathbb{R}^{2n}$, and compute

$$M_{\text{circ}}\mathbf{u} = \frac{1}{\sqrt{2n}} D^{-1} \text{diag}\left(\widehat{(M_{\text{circ}})_0}\right) D\mathbf{u} = \text{IFFT}\left(\frac{1}{\sqrt{2n}} \widehat{(M_{\text{circ}})_0} \odot \hat{\mathbf{u}}\right), \quad (10)$$

where IFFT is the inverse FFT, and \odot denotes the elementwise product. Observe that $M_{\text{toep}}\mathbf{x}$ is the first block of the result.

3 Methods

This section describes the algorithm for computing the matvec with a block triangular Toeplitz matrix \mathbf{F} . The algorithm for the case where \mathbf{F} is block lower-triangular is considered first; the upper-triangular case, which can be handled similarly, is discussed later. Recalling the shift-invariant system (5), the matrix \mathbf{F} is structured as follows:

$$\mathbf{F} = \begin{bmatrix} F_{11} & 0 & 0 & \cdots & 0 \\ F_{21} & F_{11} & 0 & \cdots & 0 \\ F_{31} & F_{21} & F_{11} & \ddots & \vdots \\ \vdots & \vdots & \ddots & \ddots & 0 \\ F_{N_t,1} & F_{N_t-1,1} & \cdots & F_{21} & F_{11} \end{bmatrix}. \quad (11)$$

\mathbf{F} has block dimension $N_t \times N_t$ and $F_{ij} \in \mathbb{R}^{N_d \times N_m}$. Recall the definitions of the sizes:

- N_t is the number of time steps;

- N_d is the spatial dimension of the data (e.g. number of sensors);
- N_m is the spatial dimension of the parameters (e.g. number of sources).

The algorithm for computing the matvec with the matrix \mathbf{F} can be broken down into two steps: 1) a setup phase where the matrix \mathbf{F} is read from file and transformed into a new matrix $\tilde{\mathbf{F}}$ with triangular Toeplitz blocks, and 2) a matvec phase where the matvec is computed using the FFT. The setup and \mathbf{F} matvec algorithms are given in Algorithms 1 and 2, respectively. In Section 3.4, the algorithm for computing the matvec with the matrix \mathbf{F}^* (which can also be applied to general block upper-triangular Toeplitz matrices) is described. The algorithm for computing the \mathbf{F}^* matvec is given in Algorithm 3. Throughout these algorithms, several index transformations are required; these, along with the notation used in the remainder of the paper, will be discussed first.

3.1 Index Transformations and Notation

The matrix \mathbf{F} is block triangular Toeplitz when written with *time-outer-space-inner* (TOSI) ordering. That is, blocks of \mathbf{F} correspond to time steps, and each block of \mathbf{F} corresponds to spatial information of the data and parameters. This index ordering can be switched to *space-outer-time-inner* (SOTI) ordering. In SOTI form, \mathbf{F} has $N_d \times N_m$ blocks; *each block* is lower-triangular Toeplitz and has size $N_t \times N_t$. The TOSI and SOTI orderings also apply to the discretized parameter vector \mathbf{m} and data vector \mathbf{d} . Different steps of the matvec algorithms involve quantities represented in either form. To denote quantities in the SOTI ordering, we use a tilde; quantities in TOSI ordering are denoted without tildes. For example, the discrete p2o map is represented by \mathbf{F} in the TOSI ordering and $\tilde{\mathbf{F}}$ in the SOTI ordering. They are related by $(\tilde{F}_{ij})_{kl} = (F_{kl})_{ij}$. Similarly, $(\tilde{\mathbf{m}}_j)_l = (\mathbf{m}_l)_j$ and $(\tilde{\mathbf{d}}_i)_k = (\mathbf{d}_k)_i$. The equation Eq. (6) is invariant under this change of index: $\tilde{\mathbf{F}}\tilde{\mathbf{m}} = \tilde{\mathbf{d}}$. In the implementation, where the matrices and vectors are stored as 1-dimensional arrays, changing between TOSI and SOTI ordering (for local quantities) corresponds to a transpose or swapaxes operation. GPU algorithms for these operations have been well studied [15, 23], and we can use them directly. Note that in an expression such as $(F_{kl})_{ij}$, the indices inside the parentheses denote the “outer” indices, and the indices outside the parentheses denote the “inner” indices. This may be a cause for confusion — remember that “outer” and “inner” refer to the index ordering of the block matrix and not where the indices appear in relation to the matrix symbol.

The matvec algorithm is designed with a multi-GPU implementation in mind. As such, the matrices and vectors are partitioned over the processors. In most cases, whether an expression refers to a local or global quantity should be evident from context. In places where there may be ambiguity, we use the notation \mathbf{v}^G to denote a global quantity and $\mathbf{v}^{L;ij}$ to denote a local quantity on the processor p_{ij} .

The Fourier transform is used throughout the algorithm. Fourier transformed quantities are denoted with hats (e.g. $\hat{\mathbf{v}}$).

3.2 Preprocessing and Partitioning of the Matrix

As mentioned in Section 2.3, the matrix \mathbf{F} is formed by computing N_m forward solves or N_d adjoint solves. When performing these solves, it is natural to work in TOSI ordering. Thus, before computing matvecs, the matrix data has to be preprocessed. The first preprocessing step is to convert the matrix to SOTI ordering. This is most easily done via a short Python script (using `numpy.reshape`, for example).

Once the matrix data is in SOTI ordering, it can be partitioned among the processors (GPUs) in the multi-GPU setup. For the distributed-memory parallelism model, a 2D grid of processors of

size $r \times c$ is assumed. In SOTI ordering, $\tilde{\mathbf{F}}$ is partitioned along the outer indices; each processor p_{ij} , $0 \leq i \leq r-1$, $0 \leq j \leq c-1$, holds the $n_d \times n_m$ sub block matrix shown in Eq. (12) (disregarding edge cases). Here, $n_d = \lceil \frac{N_d}{r} \rceil$ and $n_m = \lceil \frac{N_m}{c} \rceil$. For ease of presentation, we will only show examples of the partitioning where N_d/r and N_m/c are whole numbers.

$$\tilde{\mathbf{F}}^{L;ij} = \begin{bmatrix} \tilde{F}_{in_d, jn_m} & \tilde{F}_{in_d, jn_m+1} & \cdots & \tilde{F}_{in_d, (j+1)n_m-1} \\ \tilde{F}_{in_d+1, jn_m} & \tilde{F}_{in_d+1, jn_m+1} & \cdots & \tilde{F}_{in_d+1, (j+1)n_m-1} \\ \vdots & \vdots & \ddots & \vdots \\ \tilde{F}_{(i+1)n_d-1, jn_m} & \tilde{F}_{(i+1)n_d-1, jn_m+1} & \cdots & \tilde{F}_{(i+1)n_d-1, (j+1)n_m-1} \end{bmatrix}. \quad (12)$$

When computing matvecs, the parameter and data vectors should also be in SOTI ordering. In this case, the parameter vector is partitioned along the first row of processors $p_{0,j}$, and the data vector is partitioned along the first column of processors $p_{i,0}$. Equations (13) and (14) show an example of the vector partitioning:

$$\tilde{\mathbf{m}}^{L;0,j} = [\tilde{m}_{jn_m} \quad \tilde{m}_{jn_m+1} \quad \cdots \quad \tilde{m}_{(j+1)n_m-1}]^T, \quad (13)$$

$$\tilde{\mathbf{d}}^{L;i,0} = [\tilde{d}_{in_d} \quad \tilde{d}_{in_d+1} \quad \cdots \quad \tilde{d}_{(i+1)n_d-1}]^T. \quad (14)$$

The index-transformed matvec $\tilde{\mathbf{d}} = \tilde{\mathbf{F}}\tilde{\mathbf{m}}$ can be computed as in Eq. (15):

$$\tilde{\mathbf{d}}_k^G = \left(\tilde{\mathbf{F}}^G \tilde{\mathbf{m}}^G \right)_k = \sum_{l=0}^{n_m-1} \tilde{\mathbf{F}}_{kl}^G \tilde{\mathbf{m}}_l^G \quad (15)$$

$$\Rightarrow \tilde{\mathbf{d}}_k^{L;i,0} = \sum_{j=0}^c \sum_{l=0}^{n_m-1} \tilde{\mathbf{F}}_{kl}^{L;ij} \tilde{\mathbf{m}}_l^{L;ij}. \quad (16)$$

First, the parameter vector is broadcast down each processor column so that $\tilde{\mathbf{m}}^{L;ij} = \tilde{\mathbf{m}}^{L;0,j}$ for all $0 \leq i \leq r$. Then, each processor p_{ij} computes the local matvecs $\tilde{\mathbf{F}}_{kl}^{L;ij} \tilde{\mathbf{m}}_l^{L;ij}$. Finally, a reduction with summation is computed over each row of the processor grid.

The algorithm for matvecs with \mathbf{F}^* is structured in the same way, as shown in Eq. (17). First, the data vector is broadcast down each processor row so that $\tilde{\mathbf{d}}^{L;ij} = \tilde{\mathbf{d}}^{L;i,0}$ for all $0 \leq j \leq r$. Then, each processor p_{ij} computes the local matvecs $\tilde{\mathbf{F}}_{kl}^{*;L;ij} \tilde{\mathbf{d}}_l^{L;ij}$. Finally, a reduction with summation is computed over each column of the processor grid.

$$\tilde{\mathbf{m}}_k^G = \left(\tilde{\mathbf{F}}^{*;G} \tilde{\mathbf{d}}^G \right)_k = \sum_{l=0}^{n_d-1} \tilde{\mathbf{F}}_{kl}^{*;G} \tilde{\mathbf{d}}_l^G \quad (17)$$

$$\Rightarrow \tilde{\mathbf{m}}_k^{L;0,j} = \sum_{i=0}^r \sum_{l=0}^{n_d-1} \tilde{\mathbf{F}}_{kl}^{*;L;ij} \tilde{\mathbf{d}}_l^{L;ij}. \quad (18)$$

In either case, each local block matvec (e.g. $\tilde{\mathbf{F}}_{kl}^{L;ij} \tilde{\mathbf{m}}_l^{L;ij}$) involves a lower-triangular Toeplitz matrix. The block lower-triangular Toeplitz structure of \mathbf{F} (in the TOSI ordering) translates to the lower-triangular Toeplitz structure of each block of $\tilde{\mathbf{F}}$ (in the SOTI ordering). Recall that we only compute/store the first block column of \mathbf{F} . This corresponds to only storing the first column of each block of $\tilde{\mathbf{F}}$.

The next preprocessing step for $\tilde{\mathbf{F}}$ is to pad the first column of each of its blocks and take the Fourier transform (as explained in Section 2.4). This can be done via batched FFT methods on GPUs — we use the cuFFT library.¹⁰ We denote by $\hat{\tilde{\mathbf{F}}}$ the result of the aforementioned process. The final preprocessing step is to convert $\hat{\tilde{\mathbf{F}}}$ back to TOSI ordering. In SOTI ordering, $\hat{\tilde{\mathbf{F}}}$ consists of $N_d \times N_m$ diagonal blocks. A possible way to compute a matvec from there would be to take elementwise products and then sum over the results of each block row. This is the most natural way to formulate the algorithm, as it parallels the process in Section 2.4. However, if we convert $\hat{\tilde{\mathbf{F}}}$ to TOSI ordering, the result — denoted by $\hat{\mathbf{F}}$ — is a block diagonal matrix. After performing the corresponding reordering to the vector, the local matvec then becomes a matvec between a block diagonal matrix and vector (both consisting of complex numbers). This algorithm has the advantage that all arithmetic operations involve data that is contiguous in memory. Moreover, it can leverage routines from libraries such as cuBLAS that are well known to achieve high performance on GPUs [22]. In contrast, the former algorithm involves strided memory access patterns and has to be implemented using custom GPU kernels (see Appendix A for a discussion of this algorithm).

The conversion of local portions of $\hat{\tilde{\mathbf{F}}}$ from SOTI ordering back to TOSI ordering can be achieved with a swapaxes kernel [15].¹¹ The entries of the result, $\hat{\mathbf{F}}$, can then be stored for later use. If the same processor partitioning is used for this preprocessing/setup phase and the later matvec computations, no further reordering operations need to be done. Otherwise, the entries of $\hat{\mathbf{F}}$ need to be rearranged to match whatever partitioning of $\tilde{\mathbf{F}}$ is used in the matvec computations. Again, this is most easily done with a simple Python script. Note that all reordering operations (e.g. TOSI_TO_SOTI and SOTI_TO_TOSI) are only performed on *local* portions of matrices and vectors; no distributed communication is required.

Throughout the rest of this paper, we assume that the same partitioning is used for the preprocessing/setup phases and the matvec computations. Algorithms 1 to 3 detail the matvec algorithms. A discussion of each step of the algorithms can be found in subsequent sections.

Algorithm 1 Setup phase for computing the matvec with a block triangular Toeplitz matrix \mathbf{F} and \mathbf{F}^* .

```

1: procedure SETUP(filename,  $N_m$ ,  $N_t$ ,  $N_d$ ,  $r$ ,  $c$ )                                ▷ 2D processor index ( $i, j$ )
2:    $\tilde{\mathbf{F}} \leftarrow$  TOSI_to_SOTI( $\mathbf{F}$ )                                              ▷ Sections 3.1 and 3.2
3:    $n_d \leftarrow \lceil \frac{N_d}{r} \rceil$ ;  $n_m \leftarrow \lceil \frac{N_m}{c} \rceil$ 
4:    $\tilde{\mathbf{F}}_{kl}^{L;ij} \leftarrow$  read(filename, row_start=  $in_d$ , col_start=  $jn_m$     ▷ Section 3.2; assumes SOTI
   ordering
5:    $\hat{\tilde{\mathbf{F}}}_{kl}^{L;ij} \leftarrow$  batched_padded_fft( $\tilde{\mathbf{F}}_{kl}^{L;ij}$ )                        ▷ Section 3.3
6:
7:    $\hat{\mathbf{F}}^{L;ij} \leftarrow$  SOTI_to_TOSI( $\hat{\tilde{\mathbf{F}}}^{L;ij}$ )                                ▷ Section 3.1; add zero padding
return  $\hat{\mathbf{F}}$                                                                     ▷ Sections 3.1 and 3.2

```

¹⁰<https://docs.nvidia.com/cuda/cufft/index.html>

¹¹To be used in cuBLAS operations, the matrix should be stored in column-major order. Initially, the SOTI matrices are stored in row-major order (standard C usage). However, the swapaxes operation accomplishes both the SOTI to TOSI conversion and the switch to column-major ordering in the same kernel. Column-major storage is not needed anywhere else in the algorithm, so all other arrays are assumed to be row-major.

Algorithm 2 Matvec phase for computing the matvec with the block lower-triangular Toeplitz matrix \mathbf{F} . Assumes $\tilde{\mathbf{m}}$ in SOTI ordering (else run TOSI_to_SOTI first). Returns $\tilde{\mathbf{d}}$ in SOTI ordering. $\hat{\mathbf{F}}$ comes from running `setup`.

```

1: procedure MATVEC( $\hat{\mathbf{F}}, \tilde{\mathbf{m}}, N_m, N_t, N_d, r, c$ ) ▷ 2D processor index  $(i, j)$ 
2:    $\tilde{\mathbf{m}}_l^{L;ij} \leftarrow \text{broadcast}(\tilde{\mathbf{m}})$  ▷ broadcast input vector to all processor rows
3:    $\hat{\tilde{\mathbf{m}}}_l^{L;ij} \leftarrow \text{batched\_padded\_fft}(\tilde{\mathbf{m}}_l^{L;ij})$  ▷ Section 3.3
4:    $\hat{\mathbf{m}}^{L;ij} \leftarrow \text{SOTI\_to\_TOSI}(\hat{\tilde{\mathbf{m}}}^{L;ij})$  ▷ Section 3.3
5:    $\hat{\mathbf{d}}^{L;ij} \leftarrow \text{apply\_matrix}(\hat{\mathbf{F}}^{L;ij}, \hat{\mathbf{m}}^{L;ij})$  ▷ Section 3.3
6:    $\hat{\tilde{\mathbf{d}}}^{L;ij} \leftarrow \text{TOSI\_to\_SOTI}(\hat{\mathbf{d}}^{L;ij})$  ▷ Section 3.3
7:    $\tilde{\mathbf{d}}^{L;ij} \leftarrow \text{batched\_ifft\_and\_unpad}(\hat{\tilde{\mathbf{d}}}^{L;ij})$  ▷ Section 3.3
8:    $\tilde{\mathbf{d}}^G \leftarrow \text{reduction}(\tilde{\mathbf{d}}^{L;ij})$  ▷ Section 3.5; reduce each processor row
   return  $\tilde{\mathbf{d}}^G$  ▷ SOTI ordering Section 3.1

```

Algorithm 3 Matvec phase for computing the matvec with the block lower-triangular Toeplitz matrix \mathbf{F}^* . Assumes $\tilde{\mathbf{d}}$ in SOTI ordering (else run TOSI_to_SOTI first). Returns $\tilde{\mathbf{m}}$ in SOTI ordering. $\hat{\mathbf{F}}$ comes from running `setup`. No need to rerun setup if already run for \mathbf{F} matvecs.

```

1: procedure MATVEC( $\hat{\mathbf{F}}, \tilde{\mathbf{m}}, N_m, N_t, N_d, r, c$ ) ▷ 2D processor index  $(i, j)$ 
2:    $\tilde{\mathbf{d}}_l^{L;ij} \leftarrow \text{broadcast}(\tilde{\mathbf{d}})$  ▷ broadcast input vector to all processor columns
3:    $\hat{\tilde{\mathbf{d}}}_l^{L;ij} \leftarrow \text{batched\_padded\_fft}(\tilde{\mathbf{d}}_l^{L;ij})$  ▷ Section 3.3
4:    $\hat{\mathbf{d}}^{L;ij} \leftarrow \text{SOTI\_to\_TOSI}(\hat{\tilde{\mathbf{d}}}^{L;ij})$  ▷ Section 3.3
5:    $\hat{\mathbf{m}}^{L;ij} \leftarrow \text{apply\_matrix}(\hat{\mathbf{F}}^{L;ij}, \hat{\mathbf{d}}^{L;ij}, \text{conjugate=TRUE})$  ▷ Section 3.3
6:    $\hat{\tilde{\mathbf{m}}}^{L;ij} \leftarrow \text{TOSI\_to\_SOTI}(\hat{\mathbf{m}}^{L;ij})$  ▷ Section 3.3
7:    $\tilde{\mathbf{m}}^{L;ij} \leftarrow \text{batched\_ifft\_and\_unpad}(\hat{\tilde{\mathbf{m}}}^{L;ij})$  ▷ Section 3.3
8:    $\tilde{\mathbf{m}}^G \leftarrow \text{reduction}(\tilde{\mathbf{m}}^{L;ij})$  ▷ Section 3.5; reduce each processor row
   return  $\tilde{\mathbf{m}}^G$  ▷ SOTI ordering Section 3.1

```

3.3 Local Matvecs

After partitioning the matrix \mathbf{F} as discussed in Section 3.2, the problem has been reduced to computing the local matvecs $\widehat{\mathbf{F}}_{kl}^{L;ij} \widetilde{\mathbf{m}}_l^{L;ij}$ (or correspondingly $\widehat{\mathbf{F}}_{kl}^{*;L;ij} \widehat{\mathbf{d}}_l^{L;ij}$). As discussed in Section 3.2, when the matrices and vectors are Fourier transformed and converted back to TOSI ordering, this operation is equivalent to applying a block diagonal matrix to a vector.

Given a vector $\widetilde{\mathbf{m}}$ or $\widetilde{\mathbf{d}}$ in SOTI ordering, The first step is to pad each block with zeros and take the Fourier transform. Padding is computed with trivial custom CUDA kernels, and the batched FFTs are computed with cuFFT. After this step, the vectors are reordered to TOSI ordering.

The next step is to apply the block diagonal local matrix $\widehat{\mathbf{F}}^L$ to the local vector $\widehat{\mathbf{m}}^L$ (or correspondingly, $\widehat{\mathbf{F}}^{*;L}$ to the vector $\widehat{\mathbf{d}}^L$). This is achieved via the cuBLAS¹² `gemvStridedBatched` operation. For the case of $\widehat{\mathbf{F}}^{*;L}$ applications, the conjugate transpose of each of the diagonal blocks of $\widehat{\mathbf{F}}^L$ is applied instead. This transpose operation is not explicit; it is implicitly applied by the cuBLAS kernel when given the appropriate parameter. See Section 3.4 for a discussion on why only the matrix \mathbf{F} needs to be partitioned and stored.

After the matrix application, the resulting vector is converted back to SOTI ordering. Then, a batched IFFT is applied to this vector, and the result is unpadding (again with a trivial custom CUDA kernel). The result of this unpadding operation is the output: $\widehat{\mathbf{d}}^L$ for the \mathbf{F} matvec and $\widetilde{\mathbf{m}}^L$ for the \mathbf{F}^* matvec. Again, note that all reordering operations are only applied to *local* portions of the vectors, so no distributed communication is necessary.

3.4 Matvecs With the Transposed Matrix

Next, matvecs with the matrix \mathbf{F}^* , which is a block *upper*-triangular Toeplitz matrix, are described. One way to proceed would be to use the same algorithm as before but modify the padding before taking the FFT. However, this would require storing local parts of \mathbf{F} and \mathbf{F}^* separately, and may also require repartitioning. To avoid this extra cost, recall a key property of the Fourier transform that allows us to use the same algorithm as before with very little modification.

Recall from Section 2.4 that the first step to computing the matvec of a Toeplitz matrix M_{toep} with a vector \mathbf{x} is to form the circulant matrix M_{circ} (cf. Eq. (9)). Furthermore, recall the relation $M_{\text{circ}} = (2n)^{-1/2} D^{-1} \text{diag}\left(\widehat{(M_{\text{circ}})_0}\right) D$, where D is the DFT matrix. However, note that since the Fourier transform is a unitary operation, $D^{-1} = D^*$. This implies

$$M_{\text{circ}}^* = \begin{bmatrix} M_{\text{toep}}^* & (M')^* \\ (M')^* & M_{\text{toep}}^* \end{bmatrix} = \frac{1}{\sqrt{2n}} D^{-1} \text{diag}\left(\widehat{(M_{\text{circ}})_0}\right)^* D. \quad (19)$$

Therefore, to compute the matvec with \mathbf{F}^* , the only required modification of the previous algorithm is taking the complex conjugate transpose of the blocks of $\widehat{\mathbf{F}}^L$ before applying it to $\widehat{\mathbf{d}}$. As mentioned in Section 3.3, the conjugate transpose operation is implicitly applied by cuBLAS. This is the only change required to compute the matvec with \mathbf{F}^* , and no extra storage or partitioning is necessary. Any generic block upper-triangular Toeplitz matrix can be handled in the same way.

3.5 Reduction Over Multiple GPUs

After each processor (GPU) has computed its local matvec, the next step is to compute a reduction over either the rows (\mathbf{F} matvec) or columns (\mathbf{F}^* matvec) of the 2D processor grid. For communication between processors, NVIDIA's NCCL library is used to pass messages directly between GPUs,

¹²<https://docs.nvidia.com/cuda/cublas/>

avoiding the need for copying data to the CPU and back. Specifically, the `ncclReduce` operation can be used for this task.

Note that to achieve the best performance over multiple consecutive matvecs, all memory and other structures needed for the computation (e.g. temporary arrays, FFT plans) are allocated during the setup phase and reused over the multiple matvecs. After all matvecs are complete, this memory is freed. CUDA streams are also used to reduce kernel launch latency.

3.6 Computational Cost

Next, the theoretical time complexities for each of the steps in computing \mathbf{F} and \mathbf{F}^* matvecs listed in Section 3.5 are derived. The steps of the algorithm and their computational complexities (per GPU) are listed in Table 1. The complexities of reading the matrix from file, applying the index transformation, and moving data to the GPU are not calculated since these are one-time setup costs. The complexity of the FFT for the matrix is reported, but it is also a one-time setup cost. The complexity of each computational step is easily derived. The dimensions N_m and N_d are split among the r rows and c columns of processors, respectively, giving the local sizes n_d and n_m . The non-parallelizable dimension is N_t . The FFTs scale as $2N_t \log(2N_t)$ (factor 2 due to padding), and everything else scales as N_t . There is a factor of 8 in the communication steps since double-precision floating point numbers are used.

The computational costs given in Table 1 show that as the local sizes n_d and n_m increase (with N_t fixed, the matrix application (SBGEMV) is asymptotically the most expensive step. The dimension along which the algorithm cannot be fully parallelized is N_t . This algorithm scales as $\mathcal{O}(2N_t \log(2N_t))$ in this dimension. In contrast, a direct matvec algorithm would scale as $\mathcal{O}(N_t^2/2)$ (factor 1/2 due to the block triangular structure).

3.7 Communication-Aware Partitioning

Communication costs during the broadcast and reduction phases of the \mathbf{F} and \mathbf{F}^* matvecs present the primary barrier to the weak scalability of the matvec algorithm. To overcome the above we propose a communication-aware partitioning scheme. We use the asymptotic total communication cost $C(r, c)$ as an approximate cost model in our partitioning scheme. From Table 1, the total communication cost $C(r, c)$ for one matvec with \mathbf{F} and one with \mathbf{F}^* is given below.

$$C(r, c) := \left(\ell + \frac{8N_t n_m}{\beta} \right) \log r + \left(\ell + \frac{8N_t n_d}{\beta} \right) \log c \quad (20)$$

$$= \left(\ell + \frac{8N_t N_m}{\beta c} \right) \log r + \left(\ell + \frac{8N_t N_d}{\beta r} \right) \log c \quad (21)$$

Thus, for a given partition $p = r \times c$, we can choose r and c that minimize $C(r, c)$. We can rewrite $C(r, c)$ as

$$C(r, c) = \ell \log p + \frac{8N_t}{\beta} \left(\frac{N_m}{c} \log r + \frac{N_d}{r} \log c \right). \quad (22)$$

In the above expression, the latency term $\ell \log p$ and the bandwidth term $8N_t/\beta$ are just constant shifts or scaling of the total communication cost. As a result, it is sufficient to minimize the modified asymptotic cost function $\tilde{C}(r, c)$ defined as

$$\tilde{C}(r, c) := \frac{N_m}{c} \log r + \frac{N_d}{r} \log c. \quad (23)$$

| | Description | Computational Cost (Total work per GPU) | Notes |
|------------------|------------------|---|------------------------------------|
| Setup | FFT Matrix | $\mathcal{O}(2n_d n_m N_t \log(2N_t))$ | One time setup cost |
| | SOTI_TO_TOSI | — | One time memory operation |
| F Matvec | Broadcast Vector | $\mathcal{O}((\ell + 8N_t n_m / \beta) \log c)$ | Latency ℓ ; Bandwidth β |
| | Pad Vector | $\mathcal{O}(2n_m N_t)$ | — |
| | FFT Vector | $\mathcal{O}(2n_m N_t \log(2N_t))$ | — |
| | SOTI_TO_TOSI | — | Memory operation |
| | Apply Matrix | $\mathcal{O}(n_d n_m (N_t + 1))$ | Complex arithmetic |
| | TOSI_TO_SOTI | — | Memory operation |
| | IFFT | $\mathcal{O}(2n_d N_t \log(2N_t))$ | — |
| | Unpad Vector | $\mathcal{O}(2n_d N_t)$ | — |
| | Reduce Vector | $\mathcal{O}((\ell + 8N_t n_d / \beta) \log c)$ | Latency ℓ ; Bandwidth β |
| F* Matvec | Broadcast Vector | $\mathcal{O}((\ell + 8N_t n_d / \beta) \log c)$ | Latency ℓ ; Bandwidth β |
| | Pad Vector | $\mathcal{O}(2n_d N_t)$ | — |
| | FFT Vector | $\mathcal{O}(2n_d N_t \log(2N_t))$ | — |
| | SOTI_TO_TOSI | — | Memory operation |
| | Apply Matrix | $\mathcal{O}(n_d n_m (N_t + 1))$ | Complex arithmetic |
| | TOSI_TO_SOTI | — | Memory operation |
| | IFFT | $\mathcal{O}(2n_m N_t \log(2N_t))$ | — |
| | Unpad Vector | $\mathcal{O}(2n_m N_t)$ | — |
| | Reduce Vector | $\mathcal{O}((\ell + 8N_t n_m / \beta) \log r)$ | Latency ℓ ; Bandwidth β |

Table 1: Steps of matvec algorithm for **F** and **F*** matvecs along with their computational complexities per GPU.

Rewriting the above expression using $p = r \times c$ gives

$$\tilde{C}(r) = \frac{N_m r}{p} \log r + \frac{N_d}{r} \log \frac{p}{r} = N_m \left(\frac{r}{p} \log r + \frac{10^l}{r} \log \frac{p}{r} \right), \quad (24)$$

where $l = \log_{10}(N_d/N_m)$. Removing the overall scale factor N_m , the modified asymptotic communication cost function \tilde{C} is viewed as a function of the number of rows in the partition grid. The total number of processes p as well as the log ratio l of the global data dimension to global parameter dimension act as hyperparameters for \tilde{C} , now defined as

$$\tilde{C}(r; p, l) := \frac{r}{p} \log r + \frac{10^l}{r} \log \frac{p}{r}. \quad (25)$$

For a given value of p and l (generally known before any computations), the theoretical optimal grid configuration is the one with a number of rows that minimizes the modified asymptotic communication cost in Eq. (25). Now, there are some extra considerations: the number of processor rows r and columns c both have to be *natural numbers* multiplying to p . So, in practice, one can

minimize the real-valued function in Eq. (25) and then choose the best value for r near the real number minimizer that leads to a valid processor grid.

Another consideration that is important in the practical implementation is that of *on-node* vs. *off-node* communication costs. Communication costs between processes on the same node are generally much smaller than between processes on different nodes. For a cluster where there are k GPUs per node, communication costs along columns of the processor grid likely remain unchanged if rows are added so that $k|r$. The exception to this is if r is changed from 1 to k , in which case communication costs will definitely increase along columns. As a result, the procedure in Algorithm 4 is recommended to determine the optimal value of r . It is important to verify the optimality of the configuration through testing (at least by slightly perturbing the value of r) as hardware and network configurations can have a substantial impact on the optimal processor grid shape.

Algorithm 4 Selecting Optimal Processor Grid Shape

(p = total number of processors; $l = \log_{10}(N_d/N_m)$; k GPUs per node)

- 1: **procedure** SELECT_GRID(p, l, k)
 - 2: $\tilde{r} \leftarrow \arg \min_r \tilde{C}(r; p, l)$
 - 3: **if** $\tilde{r} = 1$ **then return** $(1, p)$
 - 4: **if** $\tilde{r} = p$ **then return** $(p, 1)$
 - 5: Choose $r \in \mathbb{N}$ close to \tilde{r} and $c \in \mathbb{N}$ close to p/\tilde{r} so that $p = rc$. Try to ensure $k|r$ and/or $k|c$.
 If $l \geq 0$, choose $r \geq c$. Else choose $r < c$.
 - return** r, c ▷ Check optimality of grid in practice.
-

Remark 1 (Remark on Scaling Tests). Strong scaling tests (where the global sizes N_m and N_d are fixed) can be performed by selecting the optimal grid shape using Algorithm 4 for each value of p that is tested. Note however, that it is not possible to keep the local sizes n_d and n_m fixed in addition to $l = \log_{10}(N_d/N_m)$ as the number of processors p is increased. The exception to this is the case where there is a square grid ($r = c$), and $p = n^2, n \in \mathbb{N}$. However, a square grid is not the optimal grid shape for any nonzero value of l , so performing weak scaling tests on a square grid is not useful for the majority of cases. Instead, if the value of l is allowed to change with p but the *sign* of l remains constant, it is possible to perform weak scaling tests. For this purpose, consider the modified asymptotic communication cost function in Eq. (24) written in terms of the local sizes n_d and n_m (which are now assumed constant)

$$\tilde{C}(r) = n_m \log r + n_d \log \frac{p}{r} = n_m \left(\log r + L \log \frac{p}{r} \right) = n_m (\log p + (1 - L) \log r), \quad (26)$$

where $L = \frac{n_d}{n_m}$. As before, the overall constant scale factor n_m and shift factor $\log p$ are removed to get the modified asymptotic communication cost for constant local sizes

$$\tilde{C}_{\text{loc}}(r) := \log r + L \log \frac{p}{r} = (1 - L) \log r. \quad (27)$$

Now, there are three cases. If $L = 1$ ($n_d = n_m$), the cost is independent of r . Thus, any grid shape can be used for weak scaling tests. If $L > 1$ ($n_d > n_m$), the cost is a monotonically decreasing function of r . Thus, a grid shape of $p \times 1$ should be used for weak scaling tests. If $L < 1$, the cost is a monotonically increasing function of r . Thus, a grid shape of $1 \times p$ should be used for weak scaling tests. For most practical applications, L is less than 1.

4 Numerical Results

The scalability and performance of the matvec algorithm were tested first on a single GPU, and then on multiple GPUs. For all GPU tests, NVIDIA A100 40 GB GPU was used, and the runtimes of the different steps in the matvec algorithm (see Table 1) were calculated. For single GPU testing, matvecs with \mathbf{F} and \mathbf{F}^* were used for different values of n_d , n_m , and N_t . For multi-GPU testing, matvecs with \mathbf{F} and \mathbf{F}^* were tested for different numbers of GPUs p . Furthermore, the CUDA kernels used in the algorithm were profiled with the `NSight Compute` software¹³ to determine their performance. For all tests, matvecs were computed between fixed, predetermined matrices and vectors. The results were compared to matvecs taken with conventional algorithms to ensure accuracy.

For the multi-GPU test, the algorithm was tested on up to 16 GPU nodes of the *Lonestar6* supercomputer at the Texas Advanced Computing Center (TACC). Each GPU node has 3 NVIDIA A100 40 GB GPUs.¹⁴ These nodes were used to determine the weak and strong scalability of our algorithm. Times for the setup phase of the algorithm are not reported, since these are one-time costs.

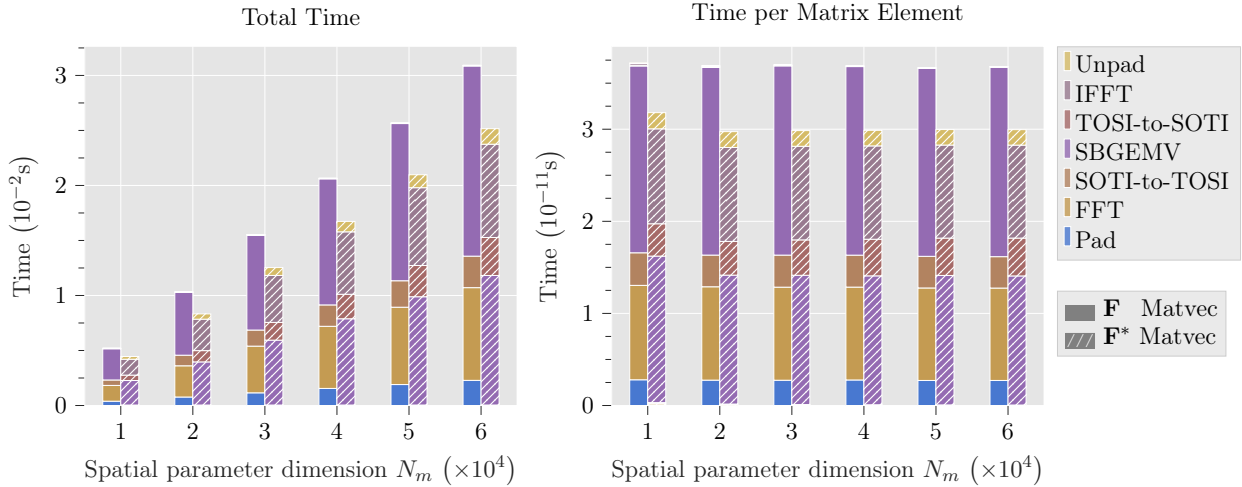


Figure 1: Total (left) and normalized (right) single-GPU scaling results for the full matvec showing the breakdown of times among different steps of the local matvec. Here, $N_t = 2,000$ and $N_d = 7$ throughout. The SBGEMV comprises the majority of the total matvec time relative to the other steps. The total computation time per element tends to a constant as the input sizes are increased.

4.1 Single-GPU Performance

Figure 1 shows the scaling results for a single GPU—aggregate and normalized by the number of local matrix elements ($2N_t n_d n_m$). The number of time steps N_t for this plot is fixed at 2,000, and the spatial data dimension (number of sensors) N_d is fixed at 7. Each bar represents a different value of the spatial parameter dimension (number of sources) N_m . The rightmost bar represents a total array size close to the memory limit of the single GPU. Each bar is separated into sections showing the times of the different portions of the local matvec. These figures show that the matrix application (SBGEMV) comprises the most time. This is to be expected since it is of size $N_t n_d n_m$.

¹³<https://developer.nvidia.com/nsight-compute>

¹⁴<https://docs.tacc.utexas.edu/hpc/lonestar6/#system-gpu>

Also note from the normalized times in Fig. 1 that as the total number of local matrix elements increases, the total cost per element remains roughly the same. Figure 2 shows the total and normalized local matvec times on a single GPU for varying values of N_m and N_d , with N_t fixed at 2,000. The expected linear scaling is observed with respect to both N_m and N_d , and we find that the total computation time per element remains roughly the same as N_m and N_d increase.

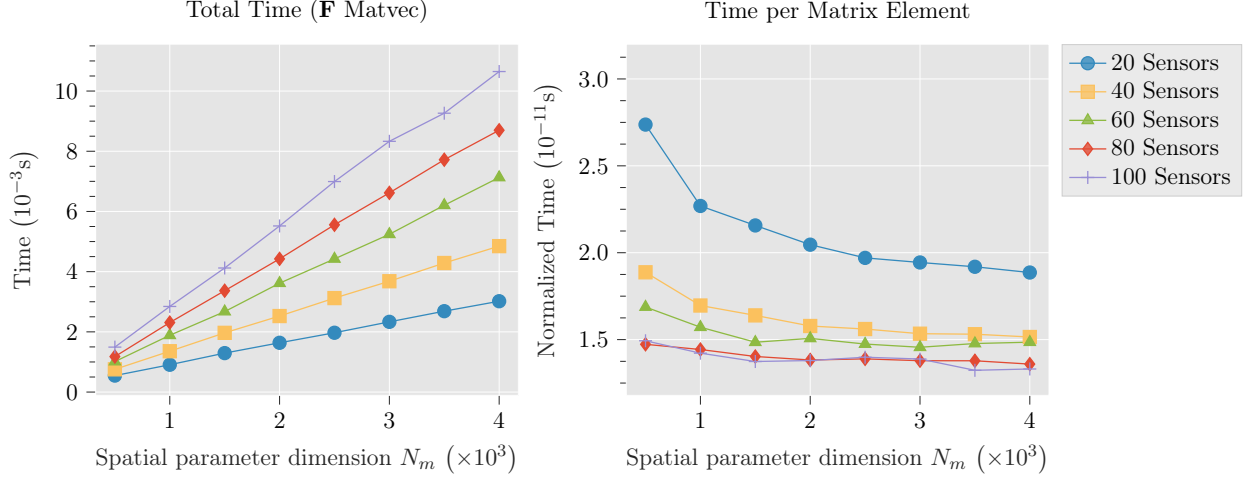


Figure 2: Total (left) and normalized (right) single-GPU scaling results for the full matvec with varying values of N_m and N_d . Here, $N_t = 2,000$ throughout. Linear scaling with respect to both N_m and N_d is observed. The total computation time per element tends to a constant as the input sizes are increased.

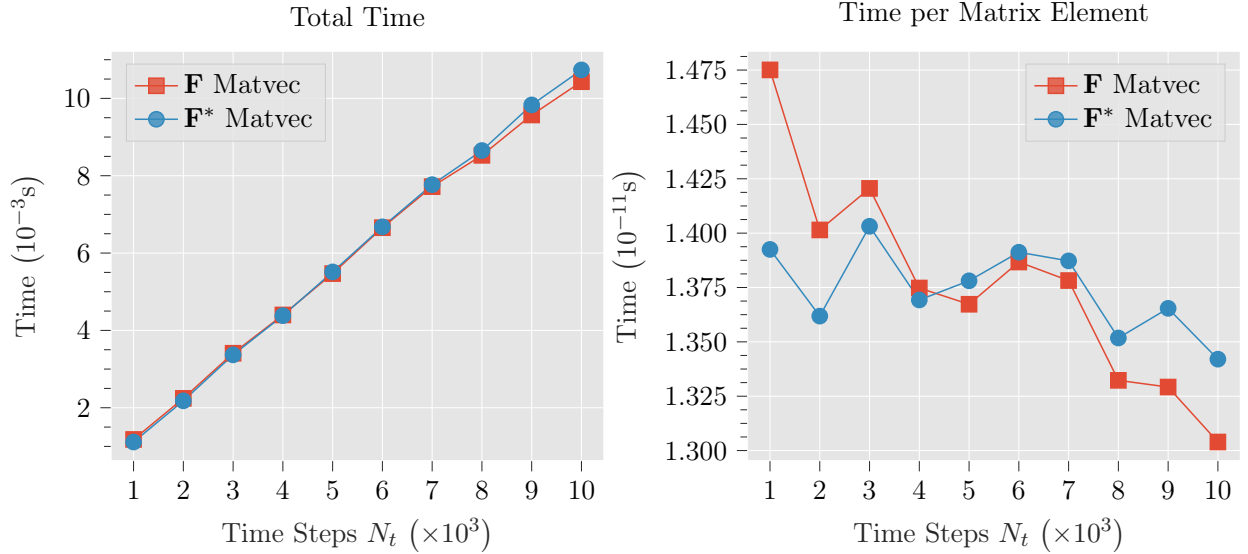


Figure 3: Total (left) and normalized (right) single-GPU scaling results for the full matvec with varying values of N_t . Here, $N_m = 800$ and $N_d = 100$ throughout. Approximate linear scaling is observed. The total computation time per element tends slightly decreases as N_t is increased.

Figure 3 shows the total and normalized local matvec times on a single GPU for varying values of N_t , with $N_m = 800$ and $N_d = 100$ fixed. According to the computational costs in Table 1, the total matvec time should scale asymptotically as $N_t \log N_t$, but practically scales as N_t for

$N_t < N_m N_d$ ($= n_d n_m$ for a single GPU). Approximate linear scaling is observed with respect to N_t , and the total computation time per element slightly decreases as N_t increases.

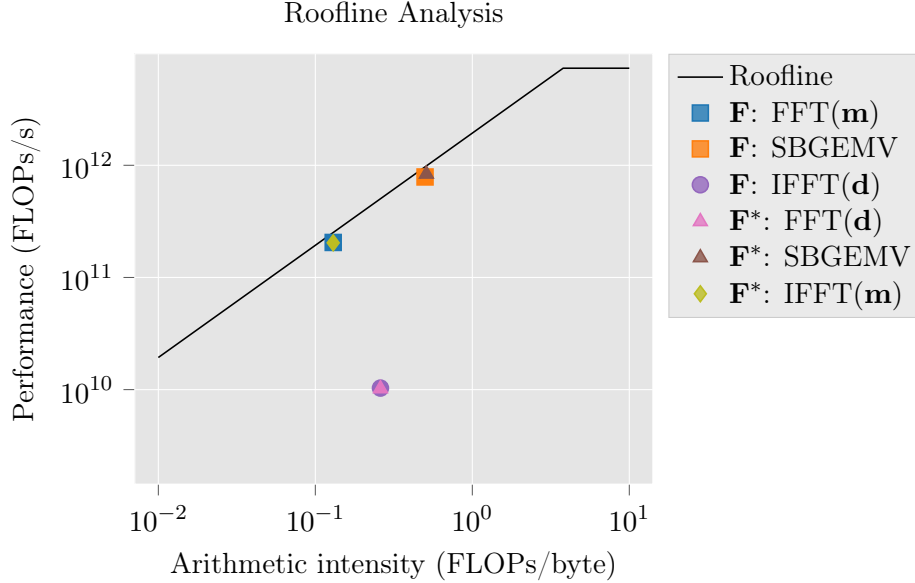


Figure 4: Roofline plots for the main kernels used in the matvec computation. All major kernels are operating at close to peak performance. Some kernels are not operating at peak performance due to small input size (they operate on a vector of size $n_d \ll n_m$); these kernels comprise less than 1% of the total runtime.

In Fig. 4, the roofline plots (obtained from `NSight Compute`) are shown. All major kernels (ReIndex not shown on the roofline plot) achieve 75–85% of the peak memory bandwidth. Note that the apparently poor performance of some kernels (FFT/IFFT(**d**)) is purely due to the small input size passed to them; these kernels account for less than 1% of the total runtime and do not pose an issue for overall performance. Roofline plots for the padding and index reordering kernels are not included since they do not have any arithmetic operations. However, these kernels are also memory bound and achieve 75–85% of the peak memory bandwidth. The major computational kernel is the SBGEMV (see Fig. 1). The theoretical FLOP count for this operation (for a single time index) is $8n_d n_m$ —the 8 is for 1 complex add and 1 complex multiply. The number of bytes used for the operation (at a single time index) is $16(n_d n_m + n_m + n_d)$ —16 bytes per complex number in the matrix and vectors. Thus, the theoretical arithmetic intensity is $n_d n_m / (2(n_d n_m + n_m + n_d))$. Assuming $n_m \ll n_m n_d$ and $n_d \ll n_m n_d$, the theoretical arithmetic intensity is 0.5—which exactly matches the observed arithmetic intensity of the SBGEMV kernels. The analysis is the same for both the **F** and **F*** matvecs.

4.2 Multi-GPU Performance

Figure 5 shows the strong and weak scaling results split over the different steps of the algorithm. As mentioned in Remark 1, a $1 \times p$ grid of GPUs was used for weak scaling, with local sizes $n_d = 10$, $N_t = 2,000$, $n_m = 20,000$. A $1 \times p$ grid was also used for strong scaling, and the global problem size was set to the maximum size that could fit on 6 GPUs ($n_d = 10$, $N_t = 2,000$, $n_m = 210,000$). Figure 5 shows that the computation costs remain constant as the number of GPUs is increased, and the communication costs increase at a sub-logarithmic rate. This is likely due to differences in on-node vs. off-node communication costs as explained in Section 3.7. Communication quickly begins to dominate the total runtime for strong scaling experiments.

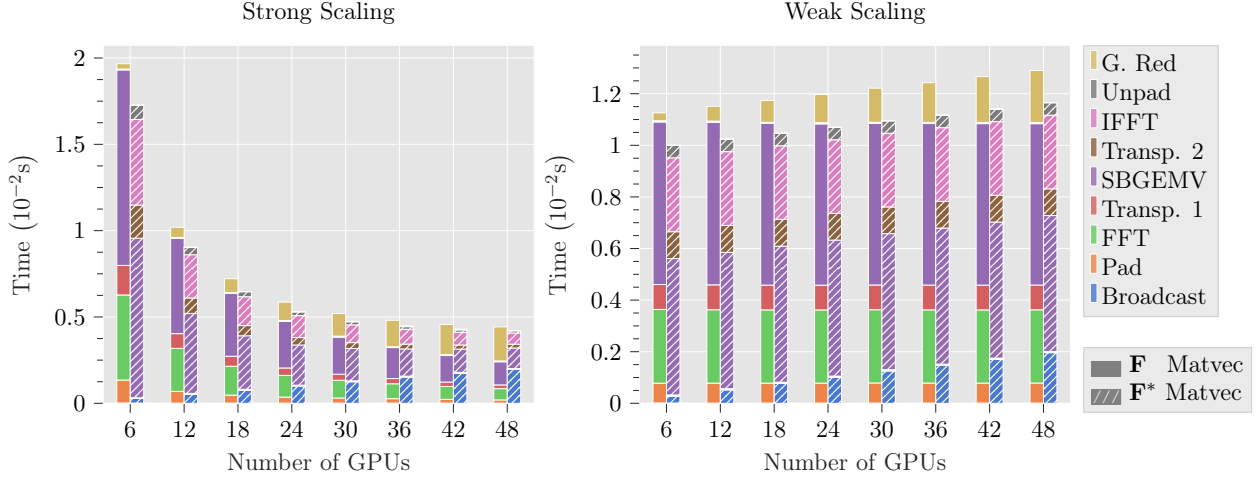


Figure 5: Strong (left) and weak (right) scaling results for the \mathbf{F} and \mathbf{F}^* matvecs on up to 48 NVIDIA A100 40 GB GPUs on TACC’s *Lonestar6* supercomputer. The GPUs are arranged in a $1 \times p$ grid, where p is the total number of GPUs.

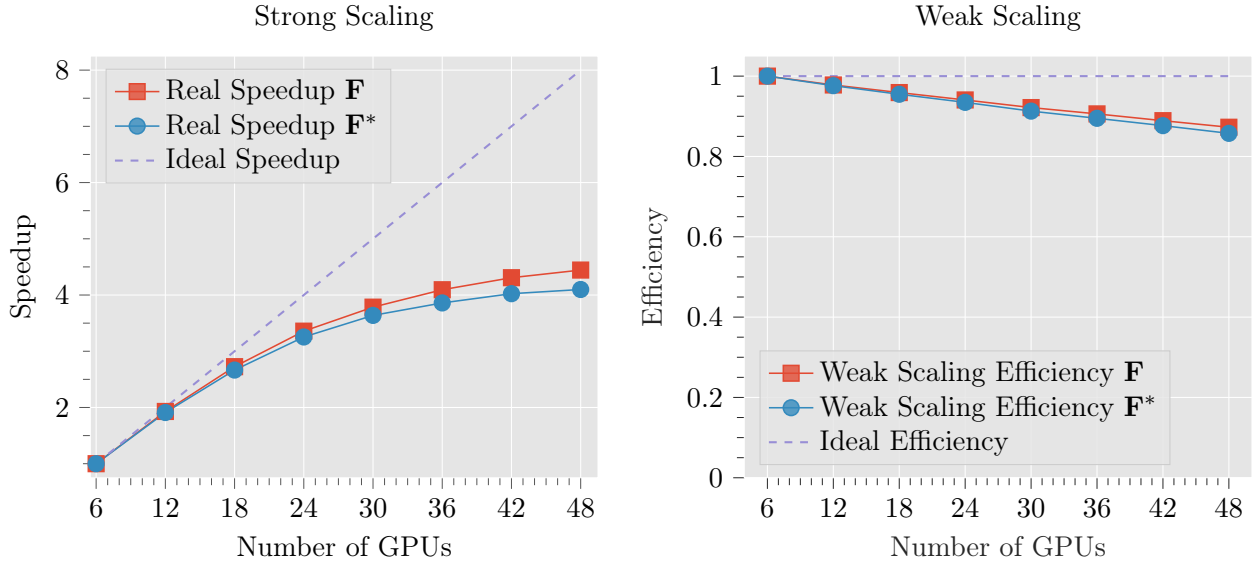


Figure 6: Strong (left) and weak (right) scaling results for the \mathbf{F} and \mathbf{F}^* matvecs on up to 48 NVIDIA A100 40 GB GPUs on TACC’s *Lonestar6* supercomputer. All tests are done on a $1 \times p$ grid, where p is the total number of GPUs. The weak scaling efficiency is controlled by the communication costs, which are growing sub-logarithmically as seen in Fig. 5. The drop in strong scaling efficiency is due to dominating communication costs and the fact that smaller problem sizes decrease GPU kernel efficiency. This effect is also observed in Fig. 2.

Figure 6 shows the results of the strong and weak scaling tests. All tests are performed on a $1 \times p$ grid, where p is the total number of GPUs. This is the optimal grid shape according to Algorithm 4 for all cases. The weak scaling efficiency is controlled by the communication costs, which are growing sub-logarithmically as seen in Fig. 5. The loss of strong scaling speedup can be explained by increased communication costs and the fact that smaller problem sizes decrease GPU kernel efficiency. This effect is also observed in Fig. 2, where decreasing the problem size increases the computational time per element of the matrix.

It is important to note that the goal of this algorithm is to enable real-time solutions of inverse

problems. From that perspective, what matters is the overall time to solution rather than scalability. In that regard, the matvec portion of this algorithm provides a significant speedup over conventional methods as mentioned in Section 2.3. A detailed comparison of the matvec runtimes for this vs. conventional algorithms will be presented in a follow-up paper. As a preview, note that for one such example, this algorithm provides a $\sim 10,000\times$ speedup over conventional methods.¹⁵

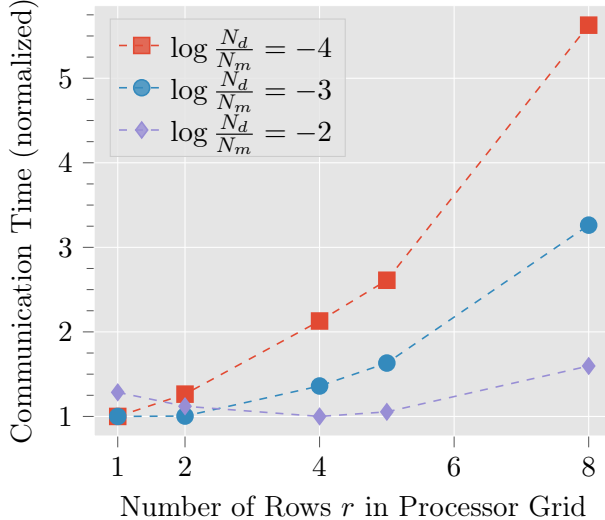


Figure 7: Communication times vs. number of rows in a processor grid with 80 GPUs for different values of $l = \log_{10}(N_d/N_m)$. Minimum times for each l value are scaled to 1. The observed minimal number of rows for each l value matches the theoretical minimal number of rows from Algorithm 4.

To compare the observed optimal grid shape for a given problem configuration to the theoretical optimal grid shape from Algorithm 4, several grid shapes for 80 GPUs were tested with different values of $l = \log_{10}(N_d/N_m)$. These tests were carried out on TACC’s *Frontera* GPU nodes (with four NVIDIA Quadro RTX 5000 GPUs per node).¹⁶ The results are shown in Fig. 7, with minimum times for each value of l scaled to 1. The observed minimal number of rows matches the theoretical number for each value of l . Only values of $l \leq -2$ are considered since this is most often the case in practice (many more parameters than data).

5 Conclusions

In the context of Hessian-based solution of inverse problems for high-dimensional parameter fields, the Hessian action on a vector typically has to be applied a large number of times. This is especially true for Hessian matrices with a slow spectral decay, i.e. where the effective rank is large compared to the parameter or data dimension, which prevents the effective use of low-rank based techniques. In such cases, and particularly for real-time inversion, it is essential that the Hessian matvec can be performed both fast and efficiently.

In this paper, we proposed an efficient and scalable multi-GPU FFT-accelerated implementation for performing matvecs of block Toeplitz systems that arise in inverse problems involving discrete shift-invariant systems. The numerical results illustrate the applicability of our approach to Hessian matvecs for large-scale parameter inversion governed by autonomous systems. For time-invariant

¹⁵The model used for this comparison is the acoustic-gravity wave equations that model tsunami dynamics [19].

¹⁶<https://docs.tacc.utexas.edu/hpc/frontera/#system-gpu>

dynamical systems, the cost of the Hessian matvec increases only linearly with the number of time steps, and near-linearly in its one-time setup cost, instead of quadratically for a naive implementation. While classical inverse algorithms with adjoint-based Hessian matvecs also scale linearly with the number of time steps, the overall cost per Hessian matvec is several orders of magnitude larger for many problems, since each Hessian matvec requires one forward and one adjoint PDE solve. This is particularly the case when (1) the governing PDEs are discretized with high-order methods, (2) the time-stepping methods for the PDE solves require small time steps for stability or accuracy, or (3) the governing system describes a multiphysics problem that is discretized with many DOFs per grid point. In those cases, our approach can outperform the classical algorithm by a factor of $1,000\times$ or larger, depending on the particular problem. Even for a problem that did not meet the prior three criteria, we showed that our approach was over $750\times$ more efficient (measured in FLOPs).

Our algorithm runs efficiently on GPUs, achieving more than 80 percent of peak bandwidth on an NVIDIA A100 GPU. Parallel scalability of the algorithm is limited only by the scaling of a vector broadcast and reduction operation that are each needed once per matvec, achieving 85-87% weak scaling efficiency on 48 A100 GPUs.

In future work, we will apply the GPU-accelerated FFT-based block Toeplitz matvec algorithm to a large-scale 3D implementation of a recently developed inverse model for tsunami early-warning [13]. The algorithm proposed here is an essential building block for solving the tsunami inverse problem, which is governed by an acoustic-gravity wave propagation model that represents an autonomous system [14]. The tsunami inversion will be applied to real-time forecasting of tsunamis from rupture events in the Cascadia subduction zone.

Acknowledgments

This research was supported in part by DOE ASCR grants DE-FOA-0002704 and DE-SC0021239. Supercomputing resources were provided by the Texas Advanced Computing Center (TACC) at UT Austin on its Frontera and Lonestar6 systems. This material is based upon work supported by the National Science Foundation Graduate Research Fellowship under Grant No. DGE 2137420.

A Appendix: Alternate Algorithm for Local Matvecs

As mentioned in Section 3.2, in SOTI ordering, $\widehat{\mathbf{F}}$ is a matrix with $N_m \times N_d$ diagonal blocks. A natural algorithm to multiply this matrix with a vector (also in SOTI ordering) would be to compute elementwise products between corresponding matrix and vector blocks and then sum over block rows. This was in fact the original implementation of the algorithm. Elementwise products and reductions over local blocks of the matrix were computed with optimized custom CUDA kernels. To handle matvecs with \mathbf{F}^* , the only necessary changes were to take the complex conjugate of the matrix elements before computing elementwise products and to reduce over columns instead of rows.

Figure 8 shows the roofline plot for this implementation of the matvec algorithm. All major kernels, including custom kernels, are operating at close to peak performance. Similarly to the plot in Fig. 4, some kernels are operating under the roofline purely due to the small input size.

Figure 9 depicts single GPU scaling results corresponding to Figs. 1 and 2 for the alternate algorithm. This figure shows that the local matvec computations are dominated by elementwise products (EWP) and local reductions (L. Red). Moreover, the overall algorithm runtimes are significantly longer than those of the algorithm presented in the main paper. The reason for this is the following: memory access patterns for the EWP are contiguous while those for the local

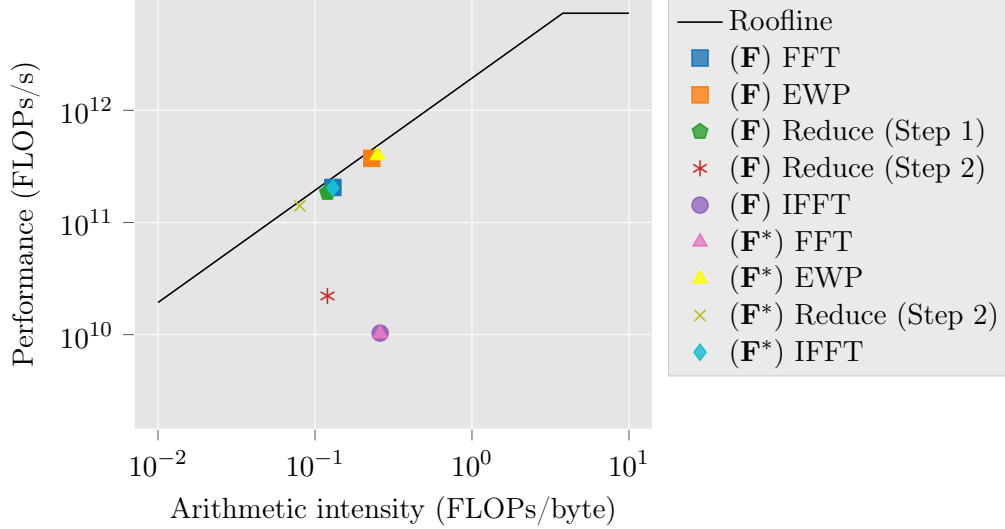


Figure 8: Roofline plots for the main kernels used in the matvec computation (alternate algorithm). All major kernels (including custom kernels) are operating at close to peak performance. Some kernels are not operating at peak performance due to small input size (they operate on a vector of size $n_d \ll n_m$); these kernels comprise less than 1% of the total runtime.

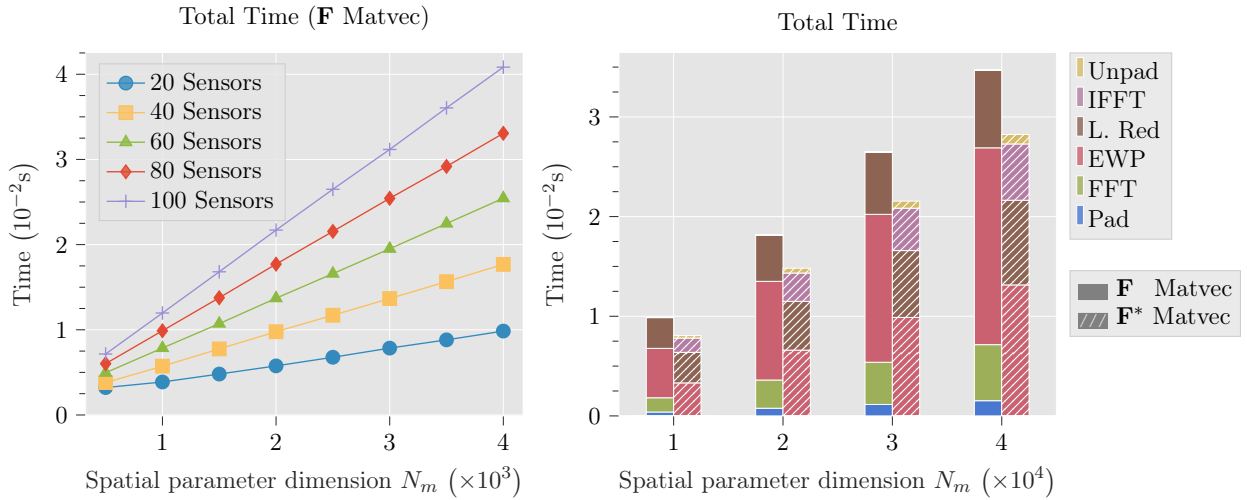


Figure 9: Single GPU scaling results for the matvec (alternate algorithm). Here, $N_t = 2,000$ for both plots. For the parameter scaling plot (right), $N_d = 7$. The extra memory usage of the alternate algorithm means that only up to $N_m = 40,000$ can be fit on the GPU. Compare to Figs. 1 and 2 (left).

reduction are strided. Strided access issues can be mitigated (and were done so) using grid-strided loops, as is evident from the fact that all kernels achieve 85–90% memory bandwidth. However, the different memory access patterns for the EWP and local reduction imply that they cannot be effectively combined into the same kernel. As a result, data has to be transferred back and forth between device global memory and cache. For the case of the EWP and reduction, there are 3 matrix read/writes and 2 vector read/writes for the EWP+local reduction. In contrast, Algorithms 2 and 3 incur 1 matrix read/write and 4 vector read/writes. The strided access pattern is accounted for by the `SOTI_TO_TOSI` and `TOSI_TO_SOTI` reindexing operations (these also explain the additional vector reads). Overall, the reduced amount of matrix-sized I/O combined with the fact that the

main computation can be offloaded to cuBLAS routines explains the superior performance of the algorithms in the main paper. In addition, the reindexing kernels operate only on vector-sized data; their runtime is negligible even though they attain a slightly lower percentage of peak bandwidth. Also, note that the alternate algorithm uses more memory overall for each matvec since intermediate results of the EWP have to be stored. As a result, the largest problem size that can fit on a single GPU is reduced for the alternate algorithm. This is why in Fig. 9 (right), only up to $N_m = 40,000$ is tested.

References

- [1] N. ALGER, T. HARTLAND, N. PETRA, AND O. GHATTAS, *Point Spread Function Approximation of High-Rank Hessians with Locally Supported Nonnegative Integral Kernels*, SIAM Journal on Scientific Computing, 46 (2024), pp. A1658–A1689.
- [2] N. ALGER, V. RAO, A. MYERS, T. BUI-THANH, AND O. GHATTAS, *Scalable Matrix-Free Adaptive Product-Convolution Approximation for Locally Translation-Invariant Operators*, SIAM Journal on Scientific Computing, 41 (2019), pp. A2296–A2328.
- [3] N. ALGER, U. VILLA, T. BUI-THANH, AND O. GHATTAS, *A Data Scalable Augmented Lagrangian KKT Preconditioner for Large-Scale Inverse Problems*, SIAM Journal on Scientific Computing, 39 (2017), pp. A2365–A2393.
- [4] I. AMBARTSUMYAN, W. BOUKARAM, T. BUI-THANH, O. GHATTAS, D. KEYES, G. STADLER, G. TURKIYYAH, AND S. ZAMPINI, *Hierarchical Matrix Approximations of Hessians Arising in Inverse Problems Governed by PDEs*, SIAM Journal on Scientific Computing, 42 (2020), pp. A3397–A3426.
- [5] B. E. BARROWES, F. L. TEIXEIRA, AND J. A. KONG, *Fast algorithm for matrix–vector multiply of asymmetric multilevel block-Toeplitz matrices in 3-D scattering*, Microwave and Optical Technology Letters, 31 (2001), pp. 28–32.
- [6] A. BEDFORD AND D. S. DRUMHELLER, *Introduction to elastic wave propagation*, Springer Nature, 2023.
- [7] L. DEMANET, P.-D. LÉTOURNEAU, N. BOUMAL, H. CALANDRA, J. CHIU, AND S. SNELSON, *Matrix probing: A randomized preconditioner for the wave-equation Hessian*, Applied and Computational Harmonic Analysis, 32 (2012), pp. 155–168.
- [8] K. GALLIVAN, S. THIRUMALAI, P. VAN DOOREN, AND V. VERMAUT, *High performance algorithms for Toeplitz and block Toeplitz matrices*, Linear Algebra and its Applications, 241 (1996), pp. 343–388.
- [9] H. P. GAVIN, *Linear time-invariant dynamical systems*, 2018. Lecture notes in System Identification, Duke University, Durham, NC, USA.
- [10] O. GHATTAS AND K. WILLCOX, *Learning physics-based models from data: perspectives from inverse problems and model reduction*, Acta Numerica, 30 (2021), pp. 445–554.
- [11] R. M. GRAY ET AL., *Toeplitz and circulant matrices: A review*, Found. Trends Commun. Inf. Theory, 2 (2006), pp. 155–239.

- [12] M. A. HASAN AND C. NEGRE, *Multiway splitting method for Toeplitz matrix vector product*, IEEE Trans. Comput., 62 (2012), pp. 1467–1471.
- [13] S. HENNEKING AND O. GHATTAS, *Toward Real-Time Tsunami Forecasting: Part 1 - Source Inversion from Near-Field Observations and an Acoustic-Gravity Wave Propagation Model*, 2024. In Preparation.
- [14] S. HENNEKING, O. GHATTAS, S. VENKAT, AND M. FERNANDO, *Fast and Efficient Bayesian Inference of High-Dimensional Parameter Fields for Autonomous Systems*, 2024. In Preparation.
- [15] J. L. JODRA, I. GURRUTXAGA, AND J. MUGUERZA, *Efficient 3d transpositions in graphics processing units*, International Journal of Parallel Programming, 43 (2015), pp. 876–891.
- [16] V. A. KAZEEV, B. N. KHOROMSKIJ, AND E. E. TYRTYSHNIKOV, *Multilevel Toeplitz matrices generated by tensor-structured vectors and convolution with logarithmic complexity*, SIAM Journal on Scientific Computing, 35 (2013), pp. A1511–A1536.
- [17] P. E. KLOEDEN AND M. RASMUSSEN, *Nonautonomous dynamical systems*, American Mathematical Society, 2011, ch. 1.
- [18] D. LEE, *Fast multiplication of a recursive block Toeplitz matrix by a vector and its application*, J. Complexity, 2 (1986), pp. 295–305.
- [19] G. C. LOTTO AND E. M. DUNHAM, *High-order finite difference modeling of tsunami generation in a compressible ocean from offshore earthquakes*, Computational Geosciences, 19 (2015), pp. 327–340.
- [20] Y. LUO, Y. LI, J. YANG, L. MA, W. HUANG, AND B. XU, *Optimization of the randomness extraction based on Toeplitz matrix for high-speed QRNG post-processing on GPU*, in 13th Int. Conf. Commun. Software Netw., 2021, pp. 261–264.
- [21] R. NAMMOUR, *Approximate multi-parameter inverse scattering using pseudodifferential scaling*, PhD thesis, Rice University, 2011.
- [22] S. D. RELTON, P. VALERO-LARA, AND M. ZOUNON, *A comparison of potential interfaces for batched blas computations*, tech. report, Manchester Institute for Mathematical Sciences, University of Manchester, 2016.
- [23] G. RUETSCH AND P. MICIKEVICIUS, *Optimizing matrix transpose in cuda*, Nvidia CUDA SDK Application Note, 18 (2009).
- [24] U. VILLA, N. PETRA, AND O. GHATTAS, *hIPPYlib: an extensible software framework for large-scale inverse problems governed by PDEs: part I: deterministic inversion and linearized Bayesian inference*, ACM Transactions on Mathematical Software, 47 (2021), pp. 1–34.
- [25] M. WAX AND T. KAILATH, *Efficient inversion of Toeplitz-block Toeplitz matrix*, IEEE Transactions on Acoustics, Speech, and Signal Processing, 31 (1983), pp. 1218–1221.
- [26] A. E. YAGLE, *A fast algorithm for Toeplitz-block-Toeplitz linear systems*, in IEEE Int. Conf. Trans. Acoust. Speech Signal Process., vol. 3, 2001, pp. 1929–1932.